NATIONAL INSTITUTE FOR FUSION SCIENCE

Macro-Particle Simulation of Collisionless
Parallel Shocks

H. Shimazu, S. Machida and M. Tanaka

RESEARCH REPORT
NIFS Series

Macro-Particle Simulation of Collisionless Parallel Shocks

H. Shimazu, S. Machida

Department of Geophysics, Kyoto University,

Sakyo-ku, Kyoto 606-01, Japan

and

Motohiko Tanaka

National Institute for Fusion Science,

Chikusa-ku, Nagoya 464-01, Japan

1

Abstract

An implicit-particle simulation of the collisionless parallel shock created at the interface between an injected beam and a stationary plasma is performed in one dimensional geometry with kinetic electrons inclusive. Electromagnetic waves with the right-hand circular polarization propagating upstream (R^- waves) are generated at the interface of the two plasmas. The R^- waves decelerate the injected beam to form a shock. The shock transition region is not monotonic but consists of two distinct regions, a pedestal and a shock ramp. The length of the transition region which contains the plasma interface is a few thousand electron skin depths. The parallel shock is non-stationary and repeats collapse and re-formation periodically in time. The right-hand circularly polarized electromagnetic waves propagating downstream (R^+ waves) are repeatedly excited at the shock ramp. Nonlinear wave-particle interaction between the beam and the R^+ waves causes wave condensation and density modulation. The R^+ waves are considered to sweep away the downstream plasma to suppress its thermal diffusion across the shock.

2

1. INTRODUCTION

Collisionless shocks are frequently observed in high-speed plasma pinches in laboratory experiemnts and at the interface of the interstellar wind and magnetized stars and planets in cosmic environments. Recent computer simulations with the hybrid-particle code have qualitatively and quantitatively improved our understanding of collisionless shocks in the solar-terrestrial circumstances. *Leroy et al.* [1982] carried out a simulation of the perpendicular shocks. They were successful in explaining a number of observational features such as existence of the reflected ions, the magnetic field profile across the shock and the Mach number dependence of the magnetic field intensity at the overshoot region.

The hybrid-particle code was also applied to study the parallel shocks [*Quest,* 1988; *Kan et al.,* 1991]. *Burgess* [1989] found a re-formation of the parallel shock in his model calculation. Since then, researches of the parallel shock have achieved a great progress mainly focusing on the re-formation process. *Winske et al.* [1990] suggested that a resonant interaction at the interface of the incoming ions and heated downstream ions was most likely the source of the waves that ultimately comprised the quasi-parallel shock (interface instability). *Scholer* [1993] and *Scholer et al.* [1993] investigated the re-formation process of the oblique quasi-parallel shocks and showed that the pulsation-like structures that steepened in upstream waves convected back toward the upstream of the shock, resulting in the shock re-formation.

A simulation of the planetary and cometary bow shocks with a stationary plasma on one-side was carried out by *Omidi and Winske* [1990]. They showed that the kinetic magnetosonic waves produced by interactions between the solar wind and the backstreaming ions steepened into shocklets.

In the previous studies mentioned above, however, electrons were assumed to be a mass-less fluid, and consequently their kinetic effects were essentially left out except through macroscopic treatment by Ohm's law. The purpose of the present paper is to investigate the roles of both the ions and electrons in the collisionless parallel shocks. We focus on the planetary parallel shocks where a super-Alfvenic solar wind and a dense

ionospheric plasma of the planet interact directly such as in Venus and Mars. Observations showed that there are two plasma boundaries in front of Venus and Mars. One is a bow shock and the other is an ionopause (magnetopause) [*Lundin et al.*, 1989; *Phillips and McComas*, 1991]. We consider that it is important to treat both the planetary bow shock and the ionopause simultaneously since their structures cannot be fully separated. Unlike previous simulations, we put a dense uniform plasma that corresponds to the planetary ionosphere in the right half of the simulation system.

In Section 2 of this paper, we describe our simulation model and parameters. A formation of the collisionless parallel shock is examined in Section 3 using the implicit-particle code. Discussions are made in Section 4, and conclusions in Section 5.

2. SIMULATION MODEL

For the purpose of clarifying the roles of both the ions and electrons in the collisionless parallel shock, we use the implicit-particle code described in *Tanaka* [1988, 1993]. The code has been tested in various circumstances such as the Alfven ion-cyclotron instability [*Tanaka*, 1993] and collisionless magnetic reconnection [*Tanaka*, 1995]. The ions are treated as macro-particles with full kinetic motion. As for the electrons, the drift-kinetic equations with the guiding-center approximation in the perpendicular motion are adopted; an inertia term is retained in the motion along the magnetic field with the magnetic moment of each electron being assumed to be conserved. In order to retain only the low-frequency (large spatial-scale) phenomena, a slightly backward time-decentered scheme is employed in the Maxwell equations and the equations of motion. The code treats one spatial dimension, three components of the particle velocities, and all the three components of the electric and magnetic fields. We do not introduce phenomenological resistivity (friction) in the equations of motion.

We emulate the solar wind by continuously injecting a super Alfvenic plasma into the simulation system from the left-side boundary. This plasma flow contacts initially at $z = \frac{1}{2}z_{max}$ with a dense stationary plasma, where z_{max} is the system size. The latter plasma corresponds to the planetary ionosphere and occupies the right half of the

4

simulation system. The simulation box is fairly large ($z_{max} = 16384c/\omega_{pe}$) to avoid an influence of the boundaries of both sides. Both the solar wind and ionosphere consist of protons (charge state $Z = 1$) and electrons. The directions of the injected solar wind and the ambient magnetic field are assumed to be exactly parallel to the simulation axis (the z-axis). Parameters of the simulation are listed in Table 1.

The simulation is performed as the initial and boundary value problem. Initially, we set the total pressure of the solar wind (dynamic pressure plus thermal pressure; $n_{SW}(m_i V_{SW}^2 + 2k_B T_{SW})$) and the thermal pressure of the ionospheric plasma ($2n_{is} k_B T_{is}$) to balance at the contact surface located at $z = 8192c/\omega_{pe}$, where k_B is the Boltzmann constant. The temperature of the ions is assumed to be equal to that of the electrons, and the temperature of the ionospheric plasma (T_{is}) is chosen the same as that of the solar wind (T_{SW}). Under the given parameters (Table 1), the initial density of the ionosphere (n_{is}) is calculated to be 17.5 times that of the solar wind (n_{SW}).

The size of the spatial cell is $\Delta z = 8c/\omega_{pe}$, and the time step is $\Delta t = 1.25 \times 10^{-2} \omega_{ci}^{-1}$, where $\omega_{pe} = (4\pi n_0 e^2/m_e)^{1/2}$ is electron plasma frequency, and $\omega_{ci} = eB_0/m_i c$ is ion cyclotron frequency. Here, c is the speed of light, e is unit charge, m_i and m_e are ion and electron mass, respectively, n_0 is number density of the upstream plasma, and B_0 is the ambient magnetic field strength. We use a frame that is stationary with the ionosphere to describe the simulation results.

3. SIMULATION RESULTS

3.1 Formation of Parallel Shock

Figure 1 depicts the formation of a parallel shock at the time $\omega_{ci}t = 75$. The velocity of the solar wind ions in Fig.1(a) begins to decrease at $z \cong z_1 = 7000c/\omega_{pe}$, which is followed by a large deceleration at the initial position of the beam-plasma interface, $z \cong z_{IP} = 8192c/\omega_{pe}$. The solar wind speed in the downstream region ($z \geq z_{IP}$) is reduced to approximately a half of the initial value $V_{SW}^{(0)} = 4V_A$. Although this speed is super-Alfvenic, the fluid velocity of the downstream plasma is nearly zero because of large concentration of the ionospheric plasma. By this time, the leading edge of the

solar wind ions reaches $z \cong 12000c/\omega_{pe}$, whereas that of the electrons almost reaches the right-side boundary (Fig.2) because of their large thermal velocities ($v_{th,e} = 7V_A$). A recovery in the parallel velocity at $10000c/\omega_{pe} < z < 12000c/\omega_{pe}$ is limited to the leading edge of the beam and does not affect the shock (cf. Figs. 1 and 7).

A part of the background (ionospheric) ions is pulled out of the downstream region and is accelerated at $z < z_{IP}$ toward the negative z-direction. But, it is interesting to note that the downstream plasma is rather well confined to the right-side of the point, $z \geq z_{IP}$, which defines the ionopause. The background ions stay at rest behind the ionopause although they are cooled along the magnetic field in the region $z < 10000c/\omega_{pe}$ as seen in Fig.1(b).

Figure 1(c) shows the total density of the ions. We can identify a well-defined, wide transition region of the collisionless parallel shock, namely, $z_1 < z < z_2$ with $z_2 \cong 9000c/\omega_{pe}$. The ionopause which is a topside boundary of the ionospheric plasma is located within the transition region, the width of which is nearly $2000c/\omega_{pe}$. The density profiles of each component in Fig.2 show that the density of the background plasma (both of the ions and electrons) rises steeply to slightly above the downstream value around $z \sim z_2$ and then overshoots to the equilibrium value at $z \geq 10000c/\omega_{pe}$.

By inspecting the density profiles carefully, it is found that a small fraction of the ionospheric ions and electrons has leaked upstream across the ionopause to form a density pedestal at $z_1 < z < z_{IP}$. The length of the pedestal is approximately a thousand electron skin depths under the present parameters. Even at this pedestal, the major ion component is not the solar wind ions but the leakage ions of the ionospheric origin, which may be a consequence of the large ionospheric plasma concentration, $n_{is}^{(0)} \sim 17n_0$. The overall density profile of the ionospheric electrons closely follows that of the ions to maintain charge neutrality. Density contribution of the solar wind electrons after penetrating into the downstream region is about two percent.

As has been found in the parallel velocity and density profiles of Fig.2 and Fig.3, the transition region of the planetary parallel shock is not monotonic but consists of two distinct regions around the ionopause, namely, the pedestal and the shock ramp. The

ionopause is included in the shock transition region as the solar wind interacts separately with the leakage and ionospheric plasmas. It is noted that, although the mass flux is conserved across the shock for the solar wind component, the momentum and energy fluxes upstream of the shock are divided between the solar wind and the ionospheric plasma in the downstream region. Thus, unless we specify the momentum and energy partitions between the solar wind and the ionospheric plasma, i.e., the specific form of the solar wind - ionospheric plasma interaction, we cannot determine the shock downstream parameters by the Rankine-Hugoniot relations for the one-fluid plasma [*Tidman and Krall*, 1971].

The perpendicular velocity of the solar wind ions V_x in Fig.1(d) is clearly modulated at $z_1 \leq z \leq z_{IP}$. In the same interval, the magnetic field B_x in Fig.1(e) shows a wavy structure. The corresponding electric field is shown in Fig.4. This electric field is right-hand circularly polarized and has the relationship with the magnetic field, $E_y \sim -(\omega/ck)B_x$, where ω and k are the frequency and wavenumber of the wave, respectively. Since E_y and B_x are in-phase in the pedestal region, we have $\omega/ck < 0$. Thus the wave is identified to be the R$^-$ wave (right-hand circularly polarized electromagnetic waves propagating to the upstream). This is consistent with the wave decomposition measurement to be shown in Sec.3.2.

With aid of Fig.4, the perpendicular velocity of the solar wind ions in Fig.1(d) is found to be following the $E \times B$ drift, $V_x \sim cE_y/B_0$. Therefore, it is said that the motion of the solar wind ions is strongly influenced by the R$^-$ waves.

3.2 Generation of Low-Frequency Waves

Figure 5 shows the time-stacked profiles of the amplitude of wave magnetic field, $(B_x^2 + B_y^2)^{1/2}$, with regard to the z coordinate. The figure depicts an overall evolution of the waves associated with the parallel shock. The reference amplitude of the ambient magnetic field, B_0, is given at the bottom-left corner. A few types of the waves are seen to be generated in the shock transition region.

The large amplitude waves generated in the $z > z_{IP}$ region and propagating downstream all the time before $\omega_{ci}t \cong 60$ are the R$^+$ waves (right-hand circularly-polarized

7

electromagnetic waves propagating to the downstream). The measured frequency and growth rate of these waves agree well with the theoretical values of the right-hand circularly-polarized resonant mode of the electromagnetic ion-beam instability [*Gary et al.*, 1984]: the observed frequency and growth rate of the maximum growing mode are $(0.31 + 0.24i)\omega_{ci}$, and those of the theory are $(0.36 + 0.28i)\omega_{ci}$ at the wavenumber $k = 3.1 \times 10^{-2}\omega_{pe}/c$. These are the waves that are generated transiently at the beam front by the fore-running solar wind ions.

Figure 5 also contains a series of magnetic waves on the upstream side of the interface of the two plasmas for $\omega_{ci}t \geq 60$. In Fig.6(a) and (b), the wave magnetic field of Fig.5 is decomposed according to helicity of the waves. For $\omega_{ci}t \geq 60$, an interaction between the solar wind and the leakage plasma from the downstream (ionosphere) excites the R$^-$ waves in the density pedestal region ($z = 7000 \sim 7700c/\omega_{pe}$), as shown in Fig.6(a). It is mentioned in passing that the linear theory of the non-resonant electromagnetic beam-plasma instability for a homogeneous plasma does not predict the R$^-$ waves. These waves could be forcedly excited by steep density gradient at the pedestal of the shock transition region, as noted by *Winske et al.* [1990]. As the result of the wave excitation, the solar wind ions are decelerated in the left half of the shock transition region, $z \leq z_{IP}$ (Fig.1a). The shock is formed for the first time at this stage as we are dealing with the initial and boundary value problem.

Figure 6(a) also shows repetition of growth and subsequent collapse of the R$^-$ waves at the shock transition region after $\omega_{ci}t \sim 75$. The collapse is seen in the figure with almost the same interval at $\omega_{ci}t = 80, 118, 143$ and 180, as indicated by triangles on the right-side edge. Since the parallel shock is associated with the R$^-$ waves, the growth and collapse of these waves will represent the dynamical evolution (re-formation) of the shock. The location of the shock is almost fixed at the initial position of the plasma interface, since we continuously inject the beam (solar wind) against the ionospheric plasma such that the pressure balance be maintained.

We also observe a different type of the electromagnetic waves in Fig.6(b), which have the R$^+$ polarization and are generated around the ionopause which is detached from the

region of R^- waves. These R^+ waves appear repeatedly and more frequently than the R^- waves. The R^+ waves have the frequency $\omega \sim 0.22\omega_{ci}$ and propagate toward downstream in the speed slower than the solar wind. The linear theory of the resonant mode [Gary et al., 1984] for the simulation parameters at $z \cong 8000c/\omega_{pe}$ yields the maximum growth $(0.27+0.30i)\omega_{ci}$ at the wavenumber $ck/\omega_{pe} = 0.044$ (the wavelength $\lambda = 143c/\omega_{pe}$). This frequency and wavelength agree well with the simulation result.

It could be these R^+ waves that are sweeping away the ionospheric plasma toward the downstream direction, since the ionopause is quite well-defined for both the ions and electrons all the time (cf. Fig.2).

3.3 Shock Collapse and Re-Formation

The particle and field quantities are shown in Fig.7 for $\omega_{ci}t = 113$ when the shock stays in a brief stationary state after the first re-formation. As in Fig.1, the parallel shock is formed at the initial position of the plasma interface (the upstream origin of the shock transition region is defined by the point where the solar wind velocity begins to decrease, or equivalently, where its density begins to increase).

At $\omega_{ci}t \cong 120$ in Fig.8, the shock starts to collapse again. The growth of the R^- waves ceases; the wave packets having the same helicity as the R^- waves drift toward the downstream direction in the reduced solar wind speed, as shown in Fig.6(a). The modulation of perpendicular velocity V_x in the shock pedestal region becomes smaller at the time of collapse in Figure 8(d) than that in Figure 7(d). The wave amplitude B_x in the pedestal region becomes consistently smaller at the time of collapse in Fig.8(e). Indeed, the phase trapping of the solar wind ions to the waves becomes obscured at the time of collapse in Fig.9(b) compared to that in Fig.9(a).

The shock collapse is also identified in the plasma quantity. The time averaged speed of the solar wind measured at $z = 8500c/\omega_{pe}$ is approximately $2.0V_A$, which decreases down to $1.3V_A$ just before the first and most evident collapse at $\omega_{ci}t \cong 80$. The solar wind speed recovers meanwhile but again is reduced to $1.7 \sim 1.8V_A$ before the subsequent collapses. This is consistent with that the shock collapse follows the growth and saturation of the waves.

Theoretically, the growth of the finite amplitude electromagnetic waves is terminated when the phase-trapping time τ_{trap} given by

$$\tau_{trap} = 2\pi(kv_\perp \omega_{ci} B_\perp/B_0)^{-1/2}, \tag{1}$$

becomes comparable to the growth time [cf. *Tanaka*, 1985], where $B_\perp$ is the amplitude of the wave magnetic field. For the observed value $B_\perp/B_0 \sim 0.5$ in Fig.7(e), we obtain $\tau_{trap} \sim 16\omega_{ci}^{-1}$. This τ_{trap} is consistent with the interval between the growth and collapse of the waves observed in the present simulation.

Figure 10 shows the time history of the number of leakage ions of the ionospheric origin (measured for $z \leq 8100c/\omega_{pe}$). If the ionospheric ions tend to diffuse thermally, the number of the leakage ions should increase. This is only true before the shock formation for $\omega_{ci}t < 75$. Once the shock is formed, the number of the leakage ions stays nearly constant; the ionospheric plasma is well conserved.

3.4 Wave Condensation and Density Modulation

Propagating wavy patterns of high density regions are seen for the solar wind in the time-stacked profile of Fig.6(c). The density modulation originates at the ionopause, $z \geq z_{IP}$ and appears periodically in time. In the phase space plot of Fig.7(a), the solar wind ions tend to pile up where their average velocity drops to a small value. If we make a close look at the solar wind speed V_z in Fig.11, it is found that a sudden drop in the solar wind speed occurs at the ionopause, and that it repeats in a time interval of $15\omega_{ci}^{-1}$.

As noticed by comparing Fig.6(b) and (c), the density modulation and the R^+ waves are well correlated. Apparently, the solar wind ions are *trapped* by the finite amplitude R^+ waves at the entrance of the ionosphere (shown by arrows in Fig.11a). A sharp cliff develops in the parallel velocity as the ions flow downstream in Fig.11(b). This time-periodic velocity modulation produces that of the solar wind density because the mass flux density must be conserved, $nV_z \sim const$. The density modulation propagates in the downstream solar wind speed, $V_z \sim 1.7V_A$, not in the phase velocity of the R^+ waves ($\sim 1.1V_A$).

10

An evidence of wave condensation in a few wavelength region is observed both in the magnetic field and the perpendicular velocity V_x at the positions indicated by arrows in Fig.11(b) and (c). In fact, the wavelength of the corresponding solar wind element (deduced from the plasma motion V_x) is reduced to a half, i.e., from $250c/\omega_{pe}$ at the ionopause in Fig.11(a) to $120c/\omega_{pe}$ at $z \sim 8300c/\omega_{pe}$ in Fig.11(b). The wave condensation proceeds to form a cluster in the (z, V_x) phase space at $\omega_{ci}t = 125$ (arrows in Fig.11c). We also find an earlier cluster at the right-side edge of Fig.11(a). After the old density modulation moves downstream, the R^+ wave generates another one near the ionopause by the solar wind-ionosphere interaction.

The above observation resembles the magnetic pulsation (clump) [*Terasawa* 1988, *Akimoto et al.* 1991]. But, the steepening of the R^+ waves in homogeneous plasmas is not observed in our simulation. Therefore, the density modulation here is attributed to condensation of the finite-amplitude R^+ waves which occurs in a few wavelengths possibly due to steep rise in the plasma density at the ionopause.

3.5 Plasma Thermalization

The parallel temperature profiles of the solar wind and ionospheric ions and electrons are shown in Fig.12 for $\omega_{ci}t = 75$. The spiky profile of the solar wind ions in the shock transition region reflects a modulation of their parallel velocity due to the wave-plasma interactions. Nevertheless, the solar wind ions are not much thermalized. On the other hand, the solar wind electrons are heated substantially as they go through the transition region. However, their energy contribution to the shock seems to be negligible because of their small mass and number density (cf. Fig.13). As for the plasma of the ionospheric origin, cooling in the pedestal region is significant for the ions. This was observed as a collimation of their parallel motion in Fig.7(b). The parallel energy is converted to the perpendicular one through the pitch-angle scattering, as will be shown in Fig.14. By sharp contrast, the temperature of the ionospheric electrons stays nearly constant.

The dynamical effects of each component on the shock formation may be better understood in the parallel energy density profiles, $\sum \frac{1}{2}mv^2 = \frac{1}{2}nm < v^2 >$, at $\omega_{ci}t = 75$ of Fig.13. As expected from the pressure balance, the solar wind energy upstream of

the shock equals to the sum of energy density of the ionospheric ions and electrons. The parallel energy density of the solar wind ions decreases as they penetrate through the shock transition region since their average velocity is reduced. (A recovery at the beam front is a transient one, as noticed before.) In the density profiles of Fig.2, the ionospheric ions and electrons stay well behind the ionopause ($z > z_{IP}$) with a slight leakage component on the upstream side. As the ionospheric ions are cooled as they approach the upstream tip of the transition region, their contribution to the energy density gradually decreases except at the very tip (this is again a transient one; cf. Figs.1 and 8). Energy contribution of the solar wind electrons is generally small as noticed above.

It is noteworthy that, to maintain the pressure balance, the amount of decrease in the energy density summed over all the ions in the shock transition region is compensated by an increase in number density, hence, energy density of the ionospheric electrons. This is consistent with charge neutrality across the shock which is achieved by electron parallel streaming (cf. Fig.17).

3.6 Flat-Topped Velocity Distribution

Figure 14 shows the velocity distribution of the ions on the upstream side of the shock transition region. The distribution of the solar wind ions for $\omega_{ci}t = 105$ swells in the perpendicular direction. This broad distribution is attributed to the velocity perturbation caused by the R$^-$ waves. After the collapse of the shock in Fig.14(b), the distribution of the solar wind ions returns to a round-shaped one, as the velocity modulation becomes weak owing to the decrease in the R$^-$ wave amplitude. The distribution becomes broader again in the perpendicular direction in Fig.14(c) due to the newly growing R$^-$ waves. On the other hand, the crescent-shaped distribution in the lower part of Fig.14(b) and (c) shows that the leakage ions are scattered in pitch-angle in the perpendicular direction.

It is quite remarkable that the parallel distribution function of the electrons observed around the upstream entrance of the shock transition region is flat-topped, as similar to the electron distribution observed in the Earth's bow shock [Feldman et al., 1983]. The electron distribution function shown in Fig.15 is mostly due to the solar wind electrons

12

since the plasma of the ionospheric origin is hardly present at the upstream tip of the transition region, $z \sim 7000c/\omega_{pe}$. This electron distribution is nearly stationary in time. The scatter plot of the solar wind electrons in Fig.16(a) shows that both heating and acceleration toward the positive z-direction are taking place in the transition region.

The heating may be attributed to resonant interaction with the ion acoustic waves. Although the ion acoustic waves are linearly stable for the simulation parameters ($T_e = T_i$, $V_{SW} < v_{th,e}$), the ion acoustic-like electrostatic oscillations with the wavelength $\lambda_z \sim 43c/\omega_{pe}$ are observed in the E_z field, which begin at the upstream entrance of the shock transition region in Fig.16(c). The trapping width D is expressed as $D \sim (2e\psi/m_e)^{1/2}$, where ψ is the wave potential. Since the observed wave electric field amounts to $2 \times 10^{-8}m_e c\omega_{pe}/e$, we obtain $D \sim 13V_A$, which is large enough to explain the observed heating.

4. DISCUSSIONS

The characteristic time of the re-formation is an important piece of information which suggests the re-formation mechanism. In *Quest* [1988] and *Omidi and Winske* [1990], the first formation time of their quasi-parallel shock was $20 \sim 30\omega_{ci}^{-1}$. In our case, it takes approximately $75\omega_{ci}^{-1}$ before the shock is first formed. This is longer than the previous works simply because a finite setup time is required in our case for the solar wind to penetrate through the ionosphere and for the ionospheric ions to leak upstream.

Similarly, the re-formation period was obtained in several studies. *Winske et al.* [1990] obtained $\tau_{ref} \sim 13\omega_{ci}^{-1}$, *Lyu and Kan* [1990] $\tau_{ref} = 6 \sim 13\omega_{ci}^{-1}$, and *Scholer* [1993] somewhat a longer period, $\tau_{ref} \sim 32\omega_{ci}^{-1}$. In our study, the re-formation period is $\tau_{ref} \sim 33\omega_{ci}^{-1}$. This is nearly double the saturation time of the R^- wave excitation between the solar wind and the ionospheric leakage ions.

It may be interesting to look at the cross-shock potential for the electrons. Figure 17(a) shows the electrostatic potential calculated by $\psi_{ES}(z) = \int^z E_z(z')dz'$ for $\omega_{ci}t = 75$. On the other hand, the total cross-shock potential, $\psi(z) = \int^z [E_z + ((\mathbf{v}/c) \times \mathbf{B})_z]dz'$, is shown in Fig.17(b). We can see a substantial potential drop in the panel (a) across the

13

ionopause, with higher potential on the upstream side. However, the total cross-shock potential is almost zero. This is interpreted that the electromagnetic force $(\mathbf{v} \times \mathbf{B})_z$ pushes the ions downstream and makes a higher potential on the downstream-side. But, the potential difference is exactly cancelled by the electron streaming (displacement) along the magnetic field, as expected from large parallel mobility of the electrons, in clear contrast to the perpendicular shock [*Leroy et al.*, 1982].

This supports that the slowdown of the solar wind in the parallel shock is caused by interactions with the electromagnetic waves, instead of the electrostatic potential. Moreover, since the main energy transfer in the parallel shock is from the parallel (beam) energy of the solar wind to the perpendicular energy of the solar wind and ionospheric ions, the dissipation associated with the parallel shock is provided by the circularly-polarized electromagnetic waves that are excited by the ion components.

It is noticeable that the number of the leakage ions from the ionosphere is predominant over that of the reflected ions in the shock pedestal region, as shown in Figs.1 and 2. This agrees with *Quest* [1988] that there are few specular reflections from the parallel shock. *Edmiston et al.* [1982] and *Lyu and Kan* [1990] showed that leakage ions are the dominant source of the backstreaming ions upstream of the quasi-parallel shock. In our implicit-particle simulation, however, the leakage ions reside stationarily on the upstream side of the ionopause. These ions do not backstream toward the upstream region.

The shock is driven by an injected beam in *Omidi and Winske* [1990] and in our simulations, rather than a piston. Differences are that, in their case, the leading edge (phase front) of the high-frequency wave packet in the upstream region oscillates back and forth in time, and that collapse of the waves (amplitude decrease) which are found in our simulation was not observed. These differences might come from the initial setting of the background plasma. In fact, the beam and the background plasma could interact continuously in the former case because of the linear density increase (slab) in the background plasma. By contrast, in the latter case, the leakage ions which correspond to the background plasma are produced in accordance with the shock formation and collapse.

Moreover, the length of the present simulation is chosen large ($16384c/\omega_{pe}$) and the

interface of the beam and the background plasma is put at the center of the system in order to avoid influences from the boundaries of both sides. We also carried out a small simulation in which the reflection (right-side) wall was placed downstream near the ionopause. In that case, the ionospheric plasma and the solar wind after being reflected were strongly thermalized and mixed in the downstream region (i.e., the shock was driven by the wall). In the MHD sense, the shock upstream parameters determine the downstream parameters. However, in the planetary shock with the ionospheric plasma, the kinetic process controls partition of momentum and energy fluxes among the downstream plasma components, which therefore determines the shock transition profile.

5. CONCLUSIONS

In this paper, the formation of the planetary parallel shock was studied using the implicit-particle code which included kinetic electrons. The interactions between the solar wind and the stationary, dense ionospheric plasma were the major issues of our interest.

We showed three types of the plasma waves that were associated with different regions of the planetary parallel shock. The first type was the right-hand circularly polarized wave propagating upstream (R^- wave). The R^- wave was excited through the interaction between the solar wind and the leakage ions from the ionosphere. Consequently, the R^- wave decelerated the solar wind ions and formed the parallel shock.

The second type of the waves was the right-hand circularly polarized wave (R^+ wave) propagating downstream which was generated by interaction between the solar wind and the dense ionospheric plasma. Another R^+ wave was generated transiently at the leading edge of the injected solar wind beam. In addition, as the third type of the waves, the shock excited the electrostatic wave which would be otherwise stable in the initial plasma condition. The R^+ electromagnetic waves were well explained by the resonant electromagnetic beam-plasma instability. But, the non-resonant beam-plasma instability did not give a solution to the R^- wave, probably because large density gradient in the shock might have excited the waves.

The shock transition region consisted of the density pedestal and the shock ramp. The length of the transition region was approximately two thousand electron skin depths; the ionopause was contained within the transition region. The shock structure were non-stationary, namely, collapse and re-formation of the parallel shock were observed. The saturation of the R^- wave lead to the collapse of the parallel shock in which the trapped solar wind ions were released and streamed down to the downstream direction. After the collapse, the leakage ions and the incoming fresh solar wind ions started an interaction to recover the parallel shock.

The solar wind electrons were heated in the pedestal of the shock, and their parallel velocity exhibited a flat-topped distribution along the magnetic field. The observed electrostatic wave which could be the ion acoustic wave was identified to be responsible for this flat-topped distribution. Despite of the finite thermal speed, the ionospheric plasma was well conserved as the excited R^+ electromagnetic wave suppressed particle diffusion.

The density modulation was observed in the solar wind, and was associated with condensation of the R^+ wave. As the repetition period of the density modulation was much smaller than that of the theory for the parametric instability [*Goldstein*, 1978], it was interpreted as due to the nonlinear wave-particle interactions. Once the density perturbations exited the *interaction* region of the R^+ wave, the wavy structure was kept and propagated at the solar wind speed due to the mass flux conservation.

In the formation of parallel shocks, the necessary dissipation is provided by the wave-particle interactions between the ions and the circularly-polarized R^- and R^+ waves excited by electromagnetic instabilities. Therefore, it is reasonable that the structure of the parallel shock varies in the characteristic time of these instabilities.

Acknowledgments

References

Akimoto, K., D. Winske, T. G. Onsager, M. F. Thomsen, and S. P. Gary, Steepening of parallel propagating hydromagnetic waves into magnetic pulsations: A simulation study, *J. Geophys. Res., 96*, 17599-17607, 1991.

Burgess, D., Cyclic behavior at quasi-parallel collisionless shocks, *Geophys. Res. Lett., 16*, 345-348, 1989.

Edmiston, J. P., C. F. Kennel, and D. Eichler, Escape of heated ions upstream of quasi-parallel shocks, *Geophys. Res. Lett., 9*, 531-534, 1982.

Feldman, W. C., R. C. Anderson, S. J. Bame, S. P. Gary, J. T. Gosling, D. J. McComas, M. F. Thomsen, G. Paschmann, and M. M. Hoppe, Electron velocity distributions near the earth's bow shock, *J. Geophys. Res., 88*, 96-110, 1983.

Gary, S. P., C. W. Smith, M. A. Lee, M. L. Goldstein, and D. W. Forslund, Electromagnetic ion beam instabilities, *Phys. Fluids, 27*, 1852-1862, 1984.

Goldstein, M. L., An instability of finite amplitude circularly polarized Alfvén waves, *Astrophys. J., 219*, 700-704, 1978.

Kan, J. R., M. E. Mandt, and L. H. Lyu, Quasi-parallel collisionless shocks, *Space Sci. Rev., 57*, 201-236, 1991.

Leroy, M. M., D. Winske, C. C. Goodrich, C. S. Wu, and K. Papadopoulos, The structure of perpendicular bow shocks, *J. Geophys. Res., 87*, 5081-5094, 1982.

Lundin, R., A. Zakharov, R. Pellinen, H. Borg, B. Hultqvist, N. Pissarenko, E. M. Dubinin, S. W. Barabash, I. Liede, and H. Koskinen, First measurements of the ionospheric plasma escape from Mars, *Nature, 341*, 609-612, 1989.

Lyu, L. H., and J. R. Kan, Ion leakage, ion reflection, ion heating and shock-front reformation in a simulated supercritical quasi-parallel collisionless shock, *Geophys. Res. Lett., 17*, 1041-1044, 1990.

Lyu, L. H., and J. R. Kan, Ion dynamics in high-Mach-number quasi-parallel shocks, *J. Geophys. Res., 98*, 18985-18997, 1993.

Omidi, N., and D. Winske, Steepening of kinetic magnetosonic waves into shocklets: Simulations and consequences for planetary shocks and comets, *J. Geophys. Res.,*

95, 2281-2300, 1990.

Phillips, J. L., and D. J. McComas, The magnetosheath and magnetotail of Venus, *Space Sci. Rev.*, *55*, 1-80, 1991.

Quest, K. B., Theory and simulation of collisionless parallel shocks, *J. Geophys. Res.*, *93*, 9649-9680, 1988.

Scholer, M., Upstream waves, shocklets, short large-amplitude magnetic structures and the cyclic behavior of oblique quasi-parallel collisionless shocks, *J. Geophys. Res.*, *98*, 47-57, 1993.

Scholer, M., M. Fujimoto, and H. Kucharek, Two-dimensional simulations of supercritical quasi-parallel shocks: Upstream waves, downstream waves, and shock re-formation, *J. Geophys. Res.*, *98*, 18971-18984, 1993.

Tanaka, M., Simulations of heavy ion heating by electromagnetic ion cyclotron waves driven by proton temperature anisotropies, *J. Geophys. Res.*, *90*, 6459-6468, 1985.

Tanaka, M., A simulation of low-frequency electromagnetic phenomena in kinetic plasmas of three dimensions, *J. Comp. Phys.*, *107*, 124-145, 1993.; *ibid.*, *79*, 209-226, 1988.

Tanaka, M., Macro-particle simulations of collisionless magnetic reconnection, *Phys. Plasmas*, *2*, 2920-2930, 1995.

Terasawa, T., Nonlinear dynamics of Alfvén waves: Interactions between ions and shock upstream waves, *Comp. Phys. Comm.*, *49*, 193-200, 1988.

Tidman, D. A., and N. A. Krall, *Shock waves in collisionless plasmas*, chap.2, John-Wiley-Interscience, New York, 1971.

Winske, D., N. Omidi, K. B. Quest, and V. A. Thomas, Re-forming supercritical quasi-parallel shocks 2. Mechanism for wave generation and front re-formation, *J. Geophys. Res.*, *95*, 18821-18832, 1990.

ratio of Alfven velocity to speed of light (V_A/c)	10^{-4}
ratio of ion cyclotron frequency to electron plasma frequency (ω_{ci}/ω_{pe})	10^{-5}
electron thermal velocity ($v_{th,e}$)	$7V_A$
solar wind velocity (V_{SW})	$4V_A$
ratio of ion (electron) thermal pressure to magnetic pressure ($\beta_i = \beta_e$)	0.49
mass ratio (m_i/m_e)	100
time step	$1.25 \times 10^{-2}\omega_{ci}^{-1}$
grid size	$8c/\omega_{pe}$

Table 1: Parameters used in the simulation.

Figure Captions

Figure 1: The phase-space (z, v_z) scatter plot of (a) the solar wind ions and (b) the ionospheric ions at the time $\omega_{ci}t = 75$. The position of the initial plasma interface (ionopause) is shown with a triangle. A dot of the ionospheric ions is 8.745 times as heavy as that of the solar wind ions. (c) The number density profile of the ions (total), (d) the averaged perpendicular velocity V_x of the solar wind ions, and (e) the magnetic perturbation B_x.

Figure 2: The number density profiles of the solar wind ions and electrons, and those of the ionospheric ions and electrons at $\omega_{ci}t = 75$ (from top to bottom).

Figure 3: The average parallel velocity $< V_z >$ of the solar wind ions and electrons, and the ionospheric ions and electrons at $\omega_{ci}t = 75$ (from top to bottom).

Figure 4: The electric field E_x and E_y, and the magnetic field B_x at the time $\omega_{ci}t = 75$.

Figure 5: The time-stacked profiles of the amplitude of wave magnetic field, $(B_x^2 + B_y^2)^{1/2}$, with regard to the space (z) coordinate. The time interval between the lines is $2.5\omega_{ci}^{-1}$.

Figure 6: (a) The time-stacked profiles of the wave magnetic field B_x decomposed according to the wave helicity: L^+ denotes the left-hand circularly polarized waves propagating downstream, and R^- the right-hand circularly polarized waves propagating upstream, (b) the B_x magnetic field which is decomposed into the R^+ and L^- waves, and (c) density of the solar wind ions. The triangles on the right-side edge of (a) show the times of the shock collapse. Each interval between the lines is $2.5\omega_{ci}^{-1}$.

Figure 7: Quantities at the time $\omega_{ci}t = 113$ after the first re-formation of the shock. The plotted quantities and formats are the same as Fig.1.

Figure 8: Quantities at the time $\omega_{ci}t = 120$ just before the shock collapse.

Figure 9: The phase angle of the wave magnetic field $B_x - B_y$ in radian (solid line), and that of the perpendicular velocity of the solar wind ions (dots) at the times $\omega_{ci}t =$ (a) 113, and (b) 120.

Figure 10: The time history of the number of the leakage ions of the ionospheric origin ($z < 8100c/\omega_{pe}$).

Figure 11: The magnetic field, B_x, the parallel and perpendicular velocities, V_z and V_x, of the solar wind (top to bottom) around the ionopause for the times $\omega_{ci}t =$ (a) 105, (b) 117.5, and (c) 125.

Figure 12: The temperature profile of the solar wind ions and electrons, the ionospheric ions and electrons (from top to bottom) at the time $\omega_{ci}t = 75$.

Figure 13: The profiles of the energy density, $\sum \frac{1}{2}mv^2$, at the time $\omega_{ci}t = 75$. For the solar wind ions (solid) and ionospheric ions (dash) in the upper frame, and for the solar wind electrons (solid) and ionospheric electrons (dash) in the lower panel. The energy density is normalized by that of the upstream solar wind.

Figure 14: The velocity distribution of the ions in the shock transition region ($z = 7000 \sim 8000c/\omega_{pe}$) at the time $\omega_{ci}t =$ (a) 105, (b) 123, and (c) 130. The upper group of dots corresponds to the solar wind ions and the lower one to the ionospheric leakage ions. A dot representing the leakage ions is 8.745 times as heavy as that of the solar wind ions.

Figure 15: The parallel velocity distribution functions of the electrons at $\omega_{ci}t = 75$. The dashed line corresponds to the distribution measured for $z = 5000 \sim 5200c/\omega_{pe}$ (upstream), and the solid line for $z = 7000 \sim 7200c/\omega_{pe}$ (downstream).

Figure 16: The phase space scatter plot of the parallel velocity for (a) the solar wind electrons, (b) the ionospheric electrons, and (c) the electrostatic component of the

electric field E_z at the time $\omega_{ci}t = 75$.

Figure 17: The cross-shock potentials, (a) the electrostatic part, $\int^z E_z(z')dz'$, and (b) the total potential, $\int^z (\mathbf{E} + (\mathbf{v}/c) \times \mathbf{B})_z dz'$, at $\omega_{ci}t = 75$.
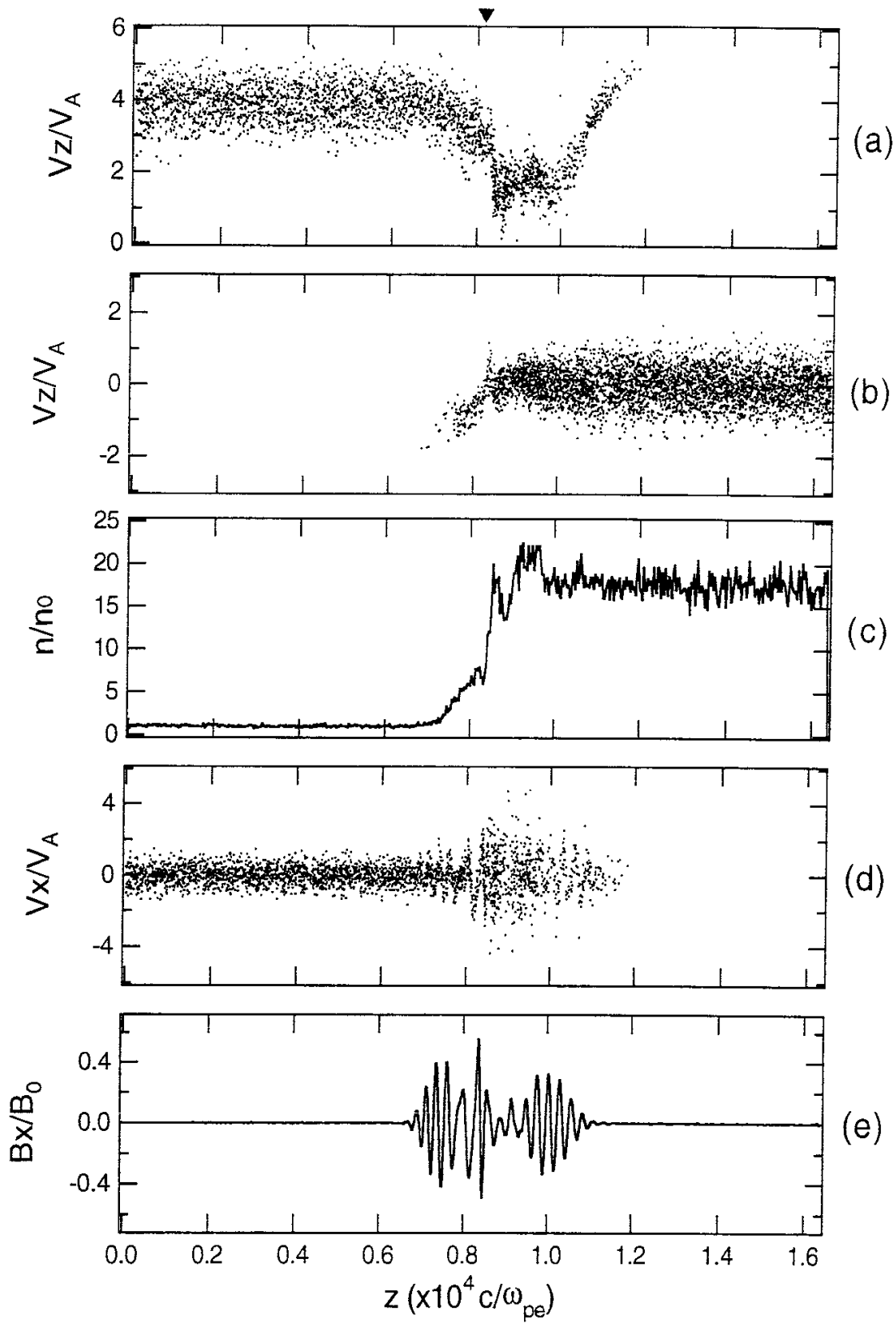
Figure 1.
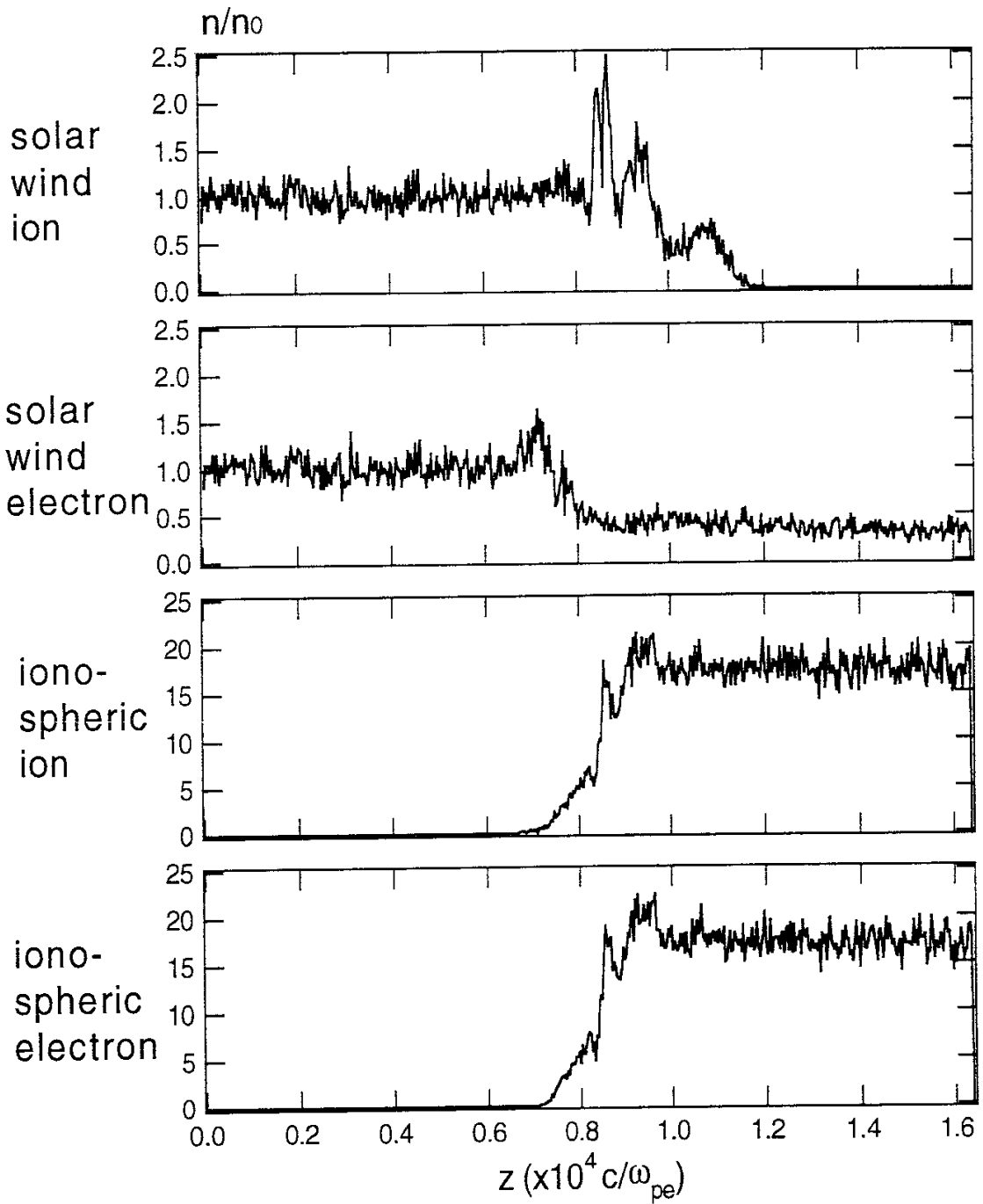
Figure 2.
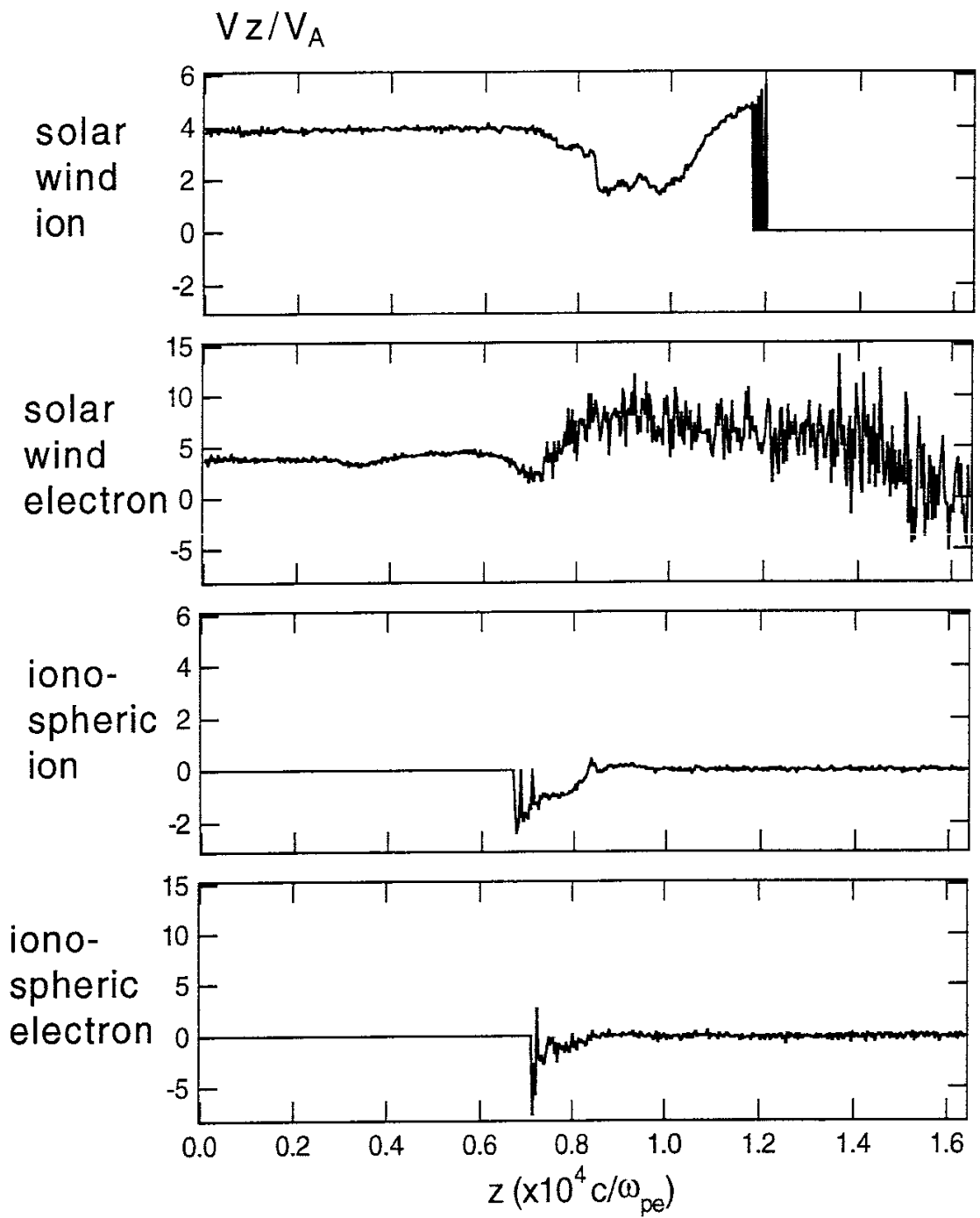
Figure 3.
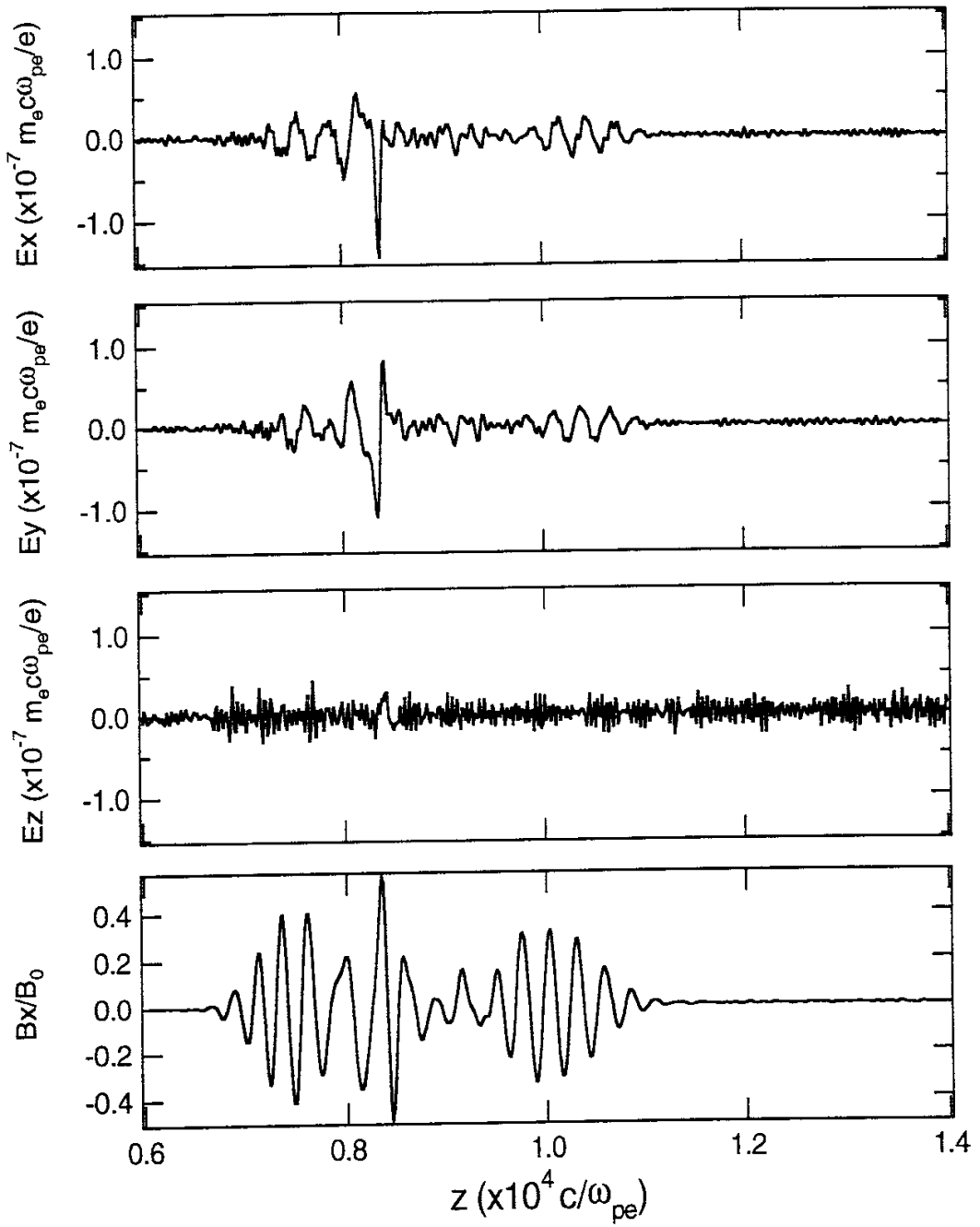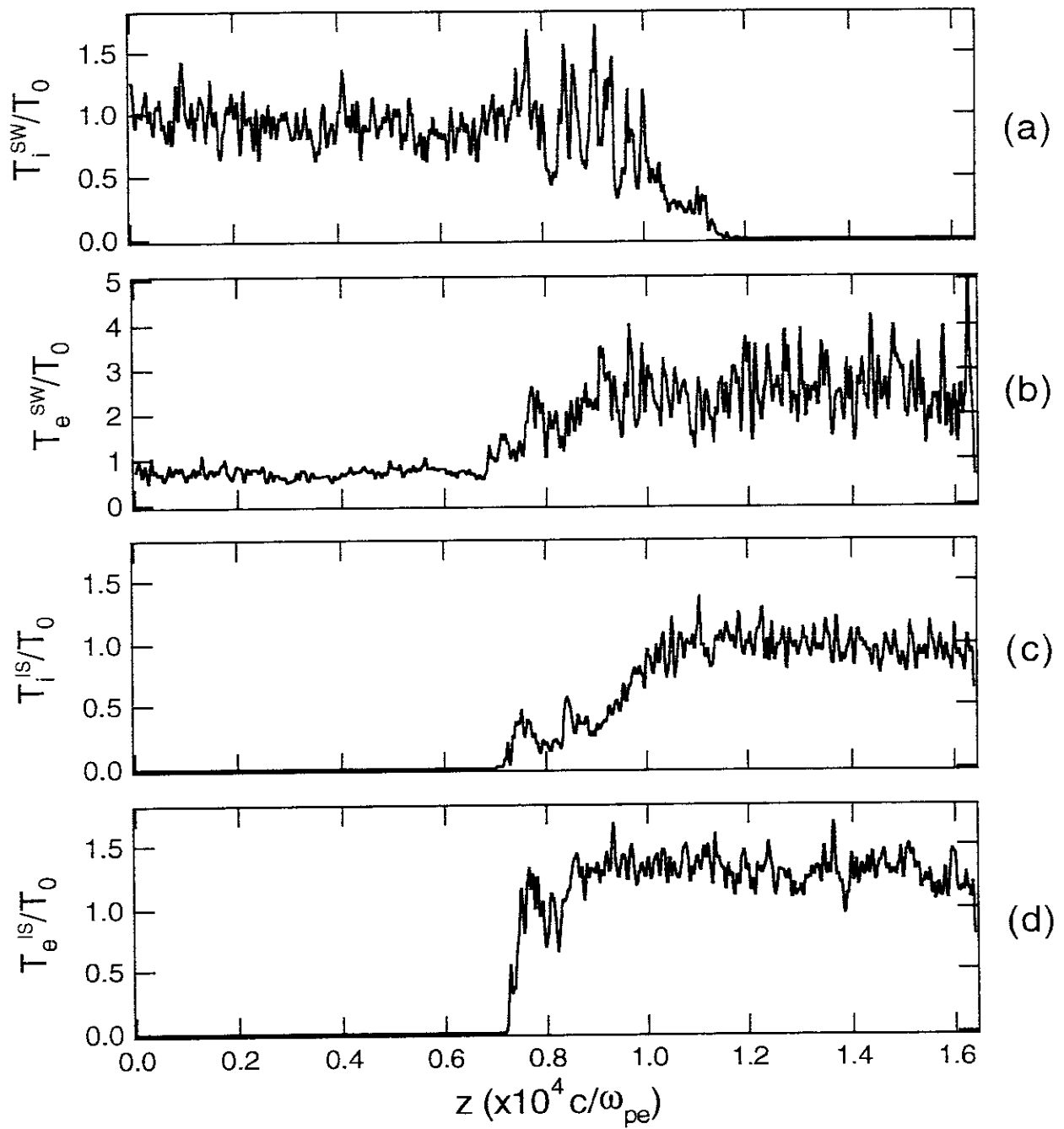
Figure 4.
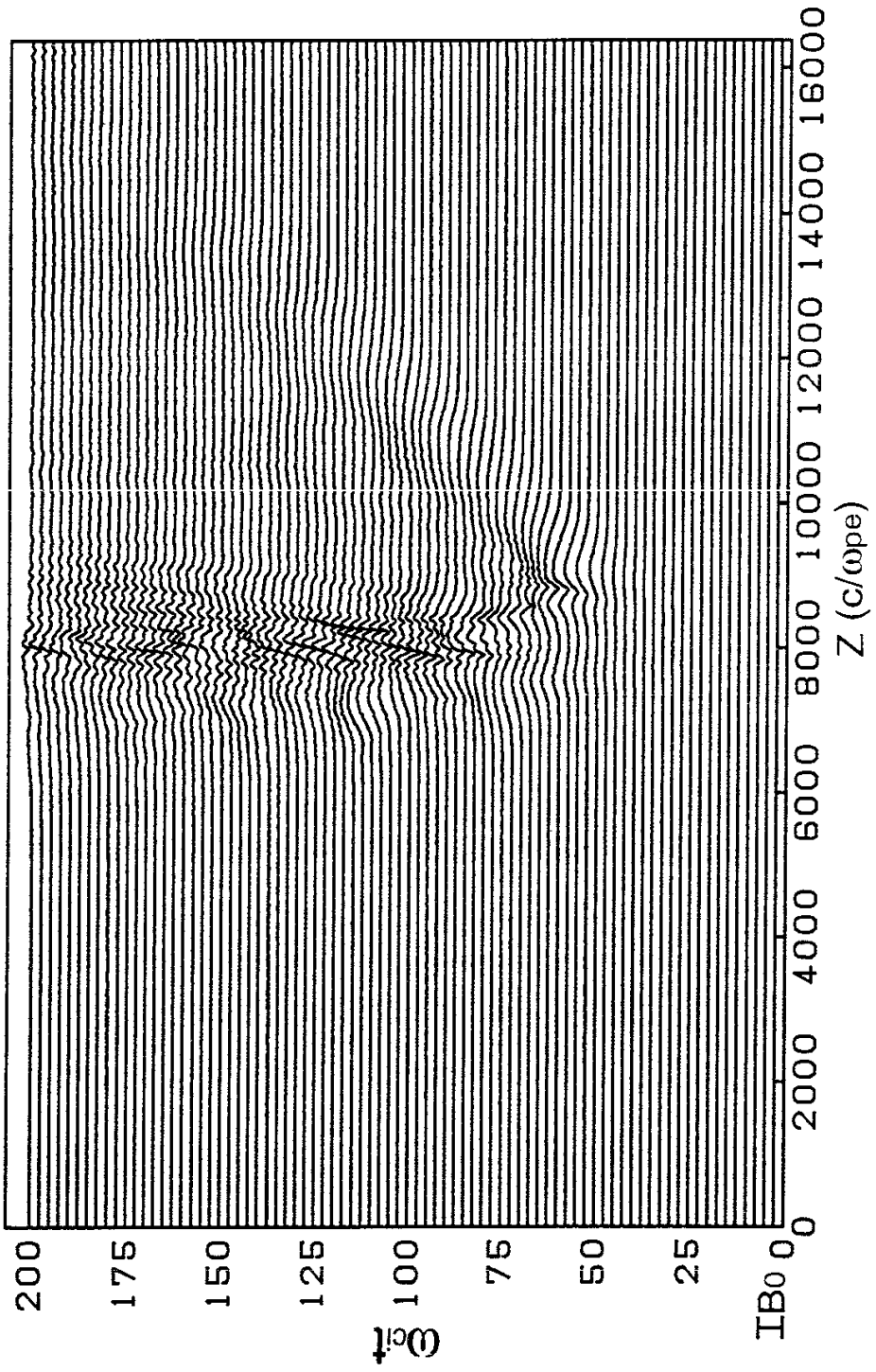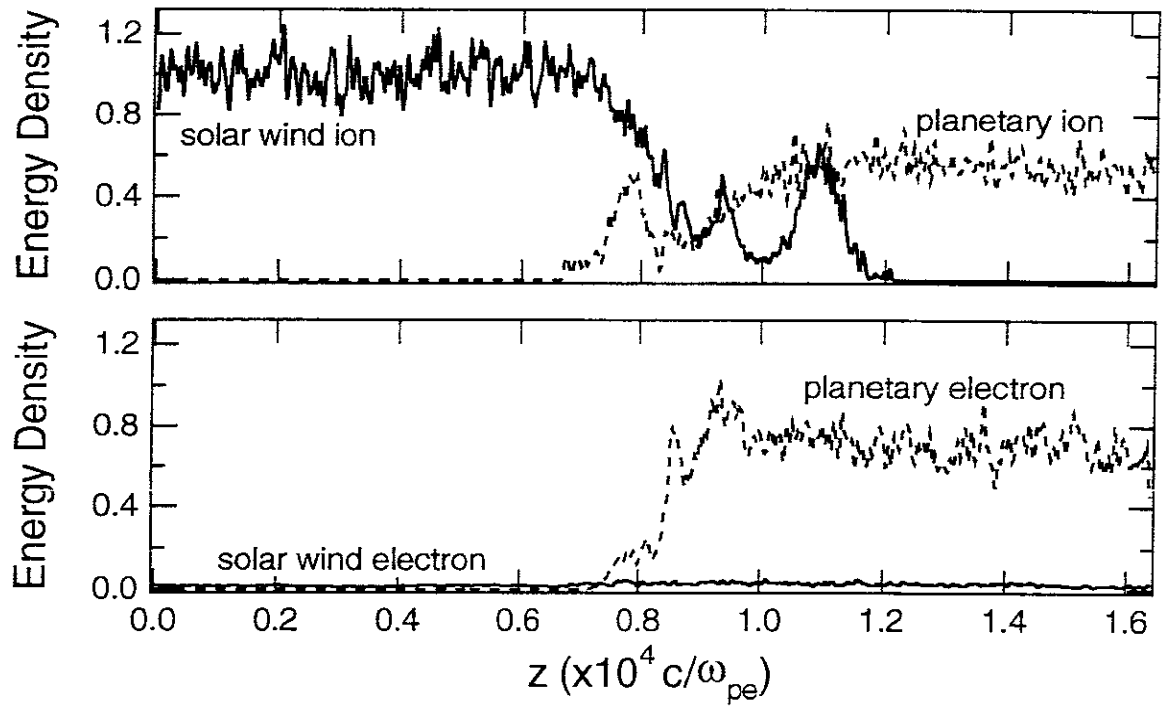
Figure 5.
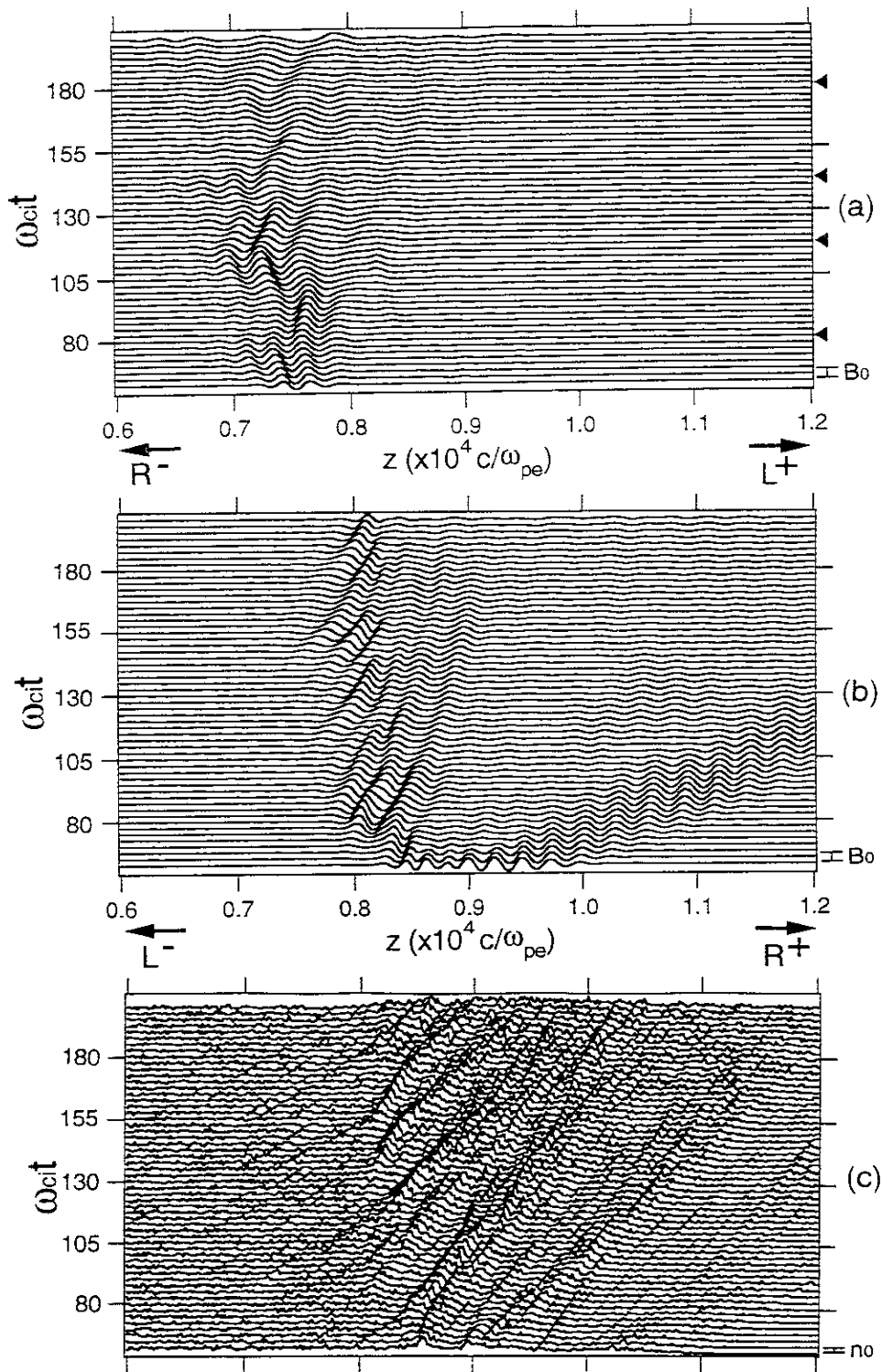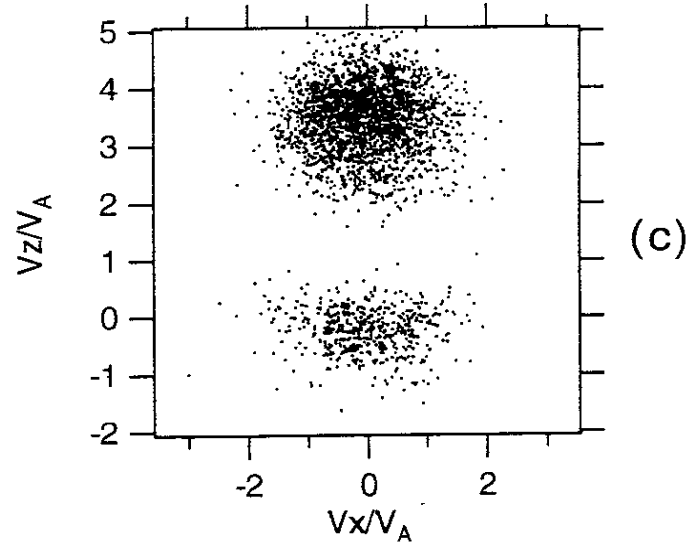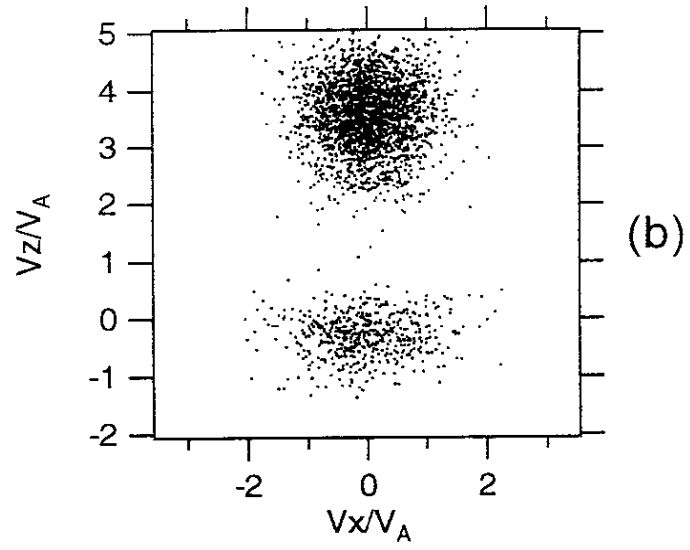
Figure 6.
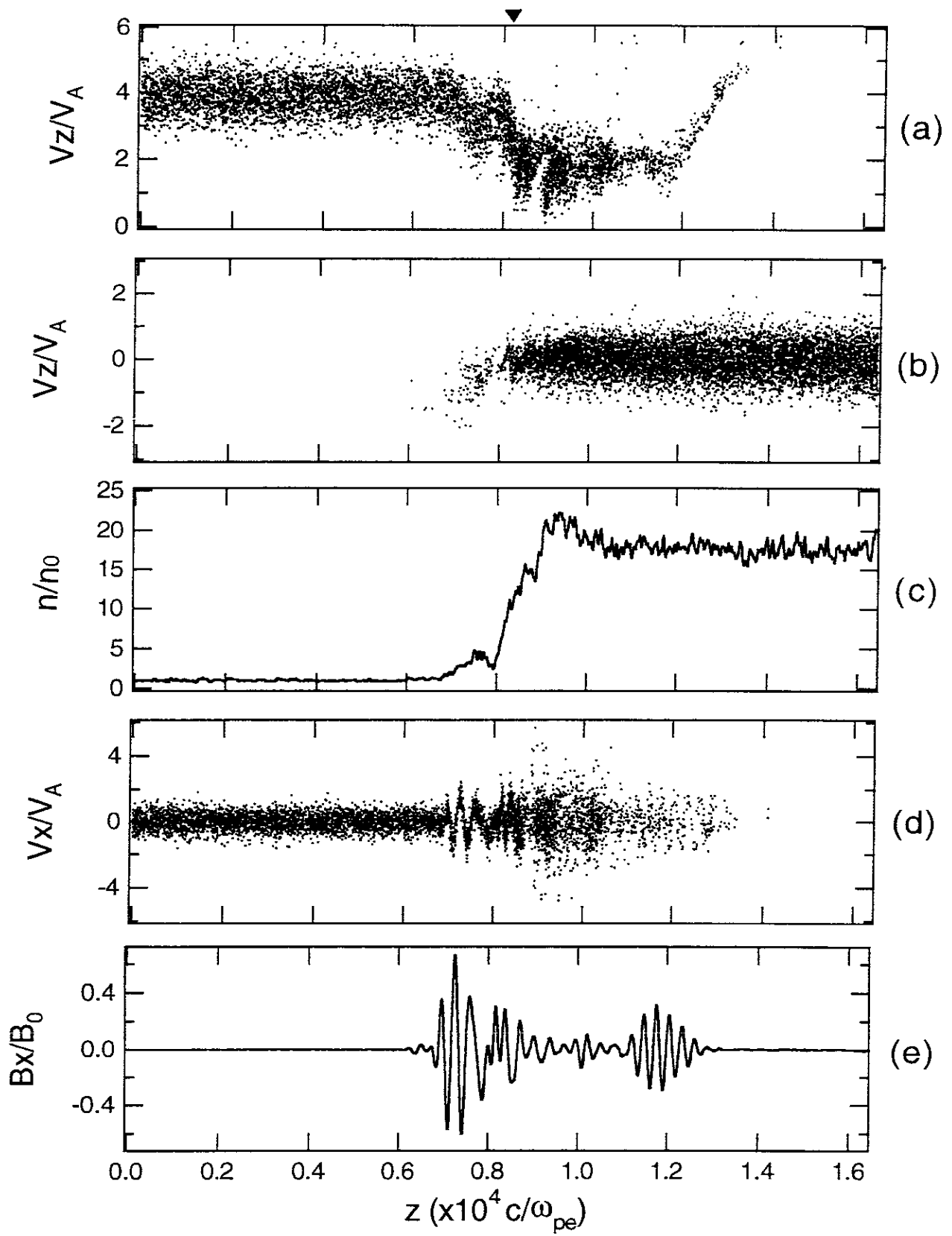
Figure 7.
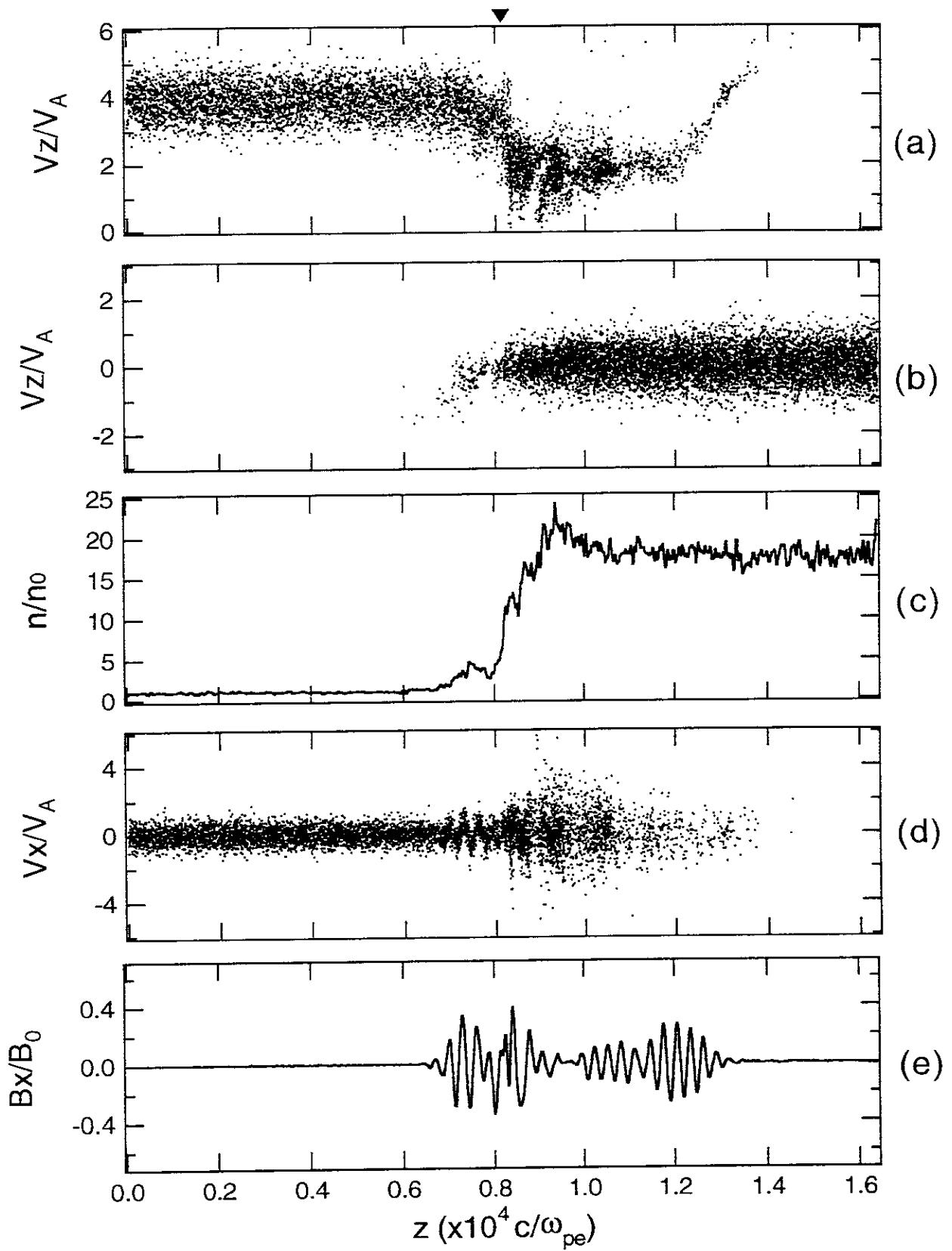
Figure 8.
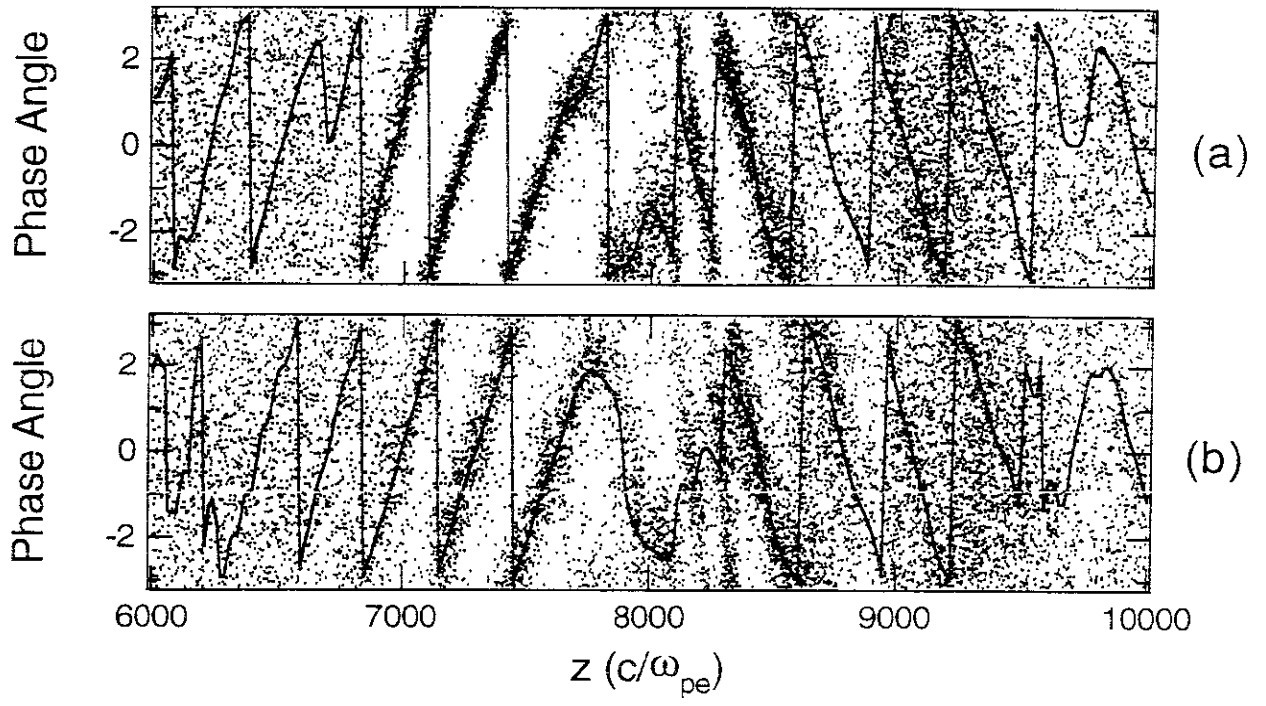
Figure 9.
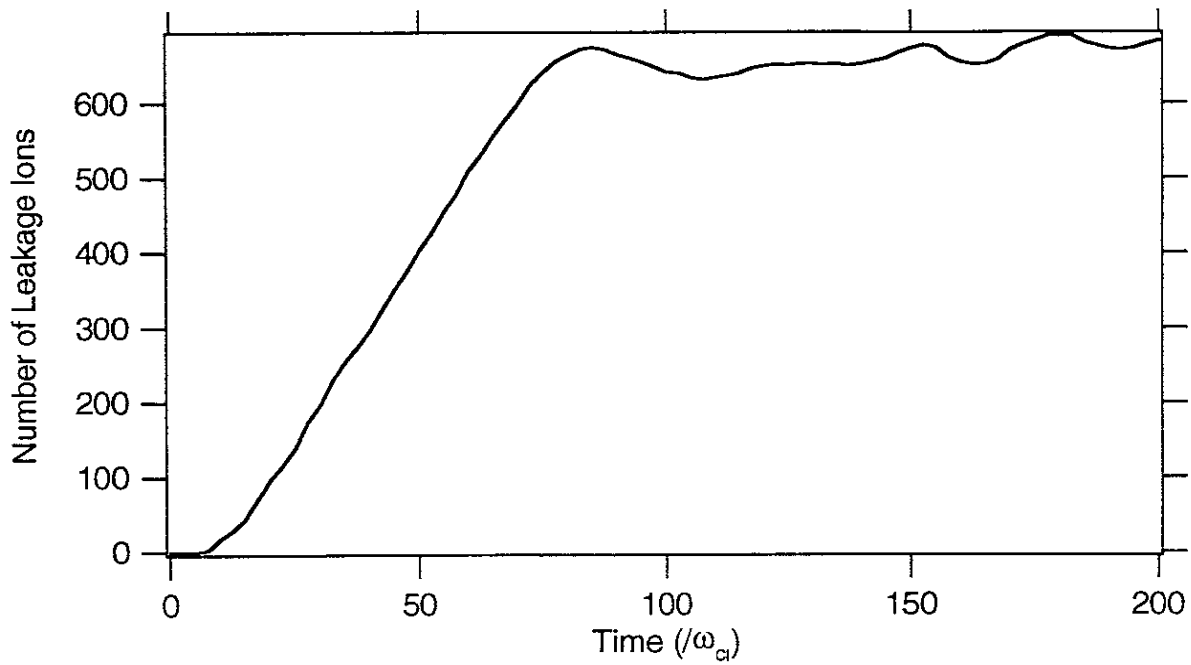
Figure 10.
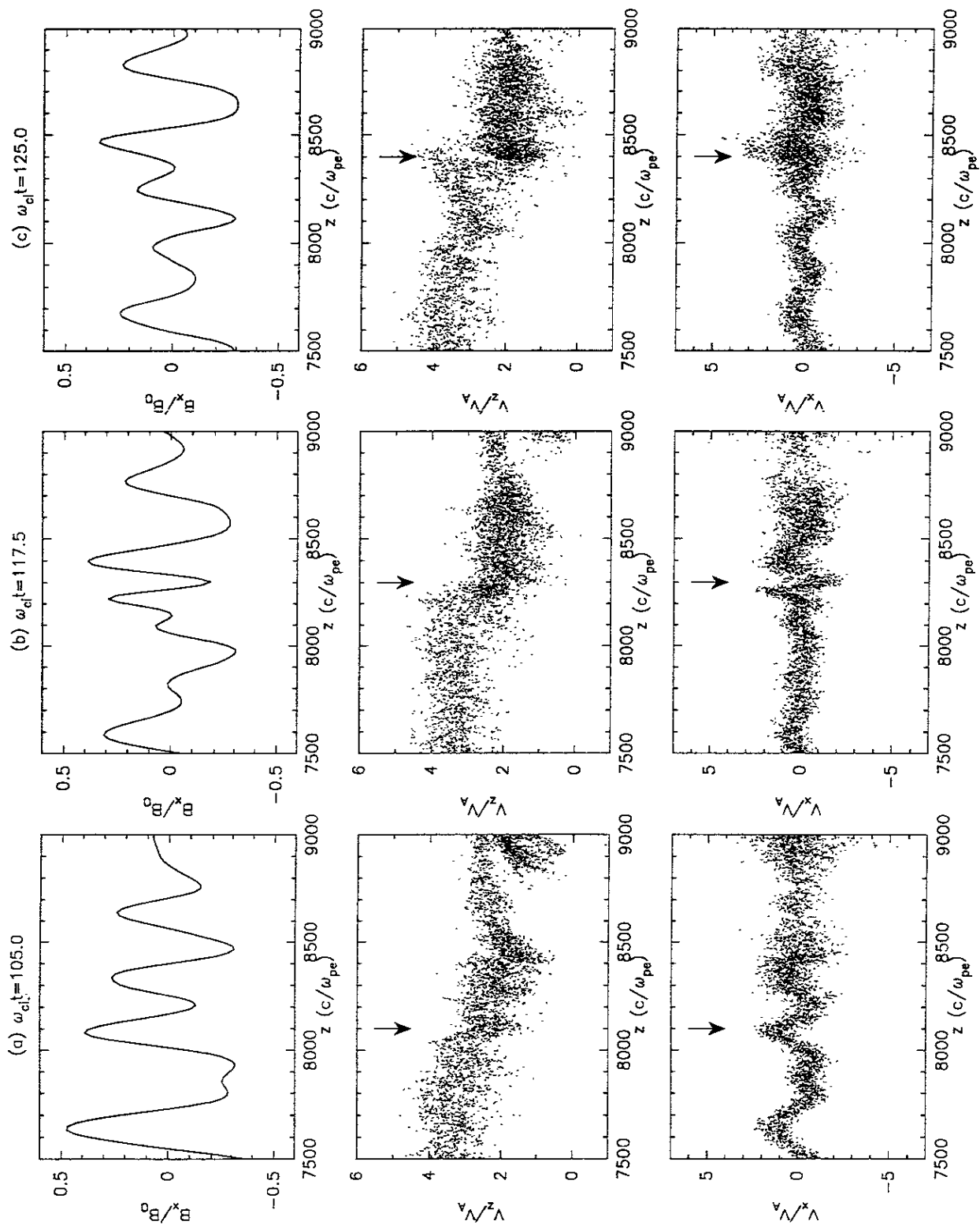
Figure 11.

Figure 12.

Figure 13.
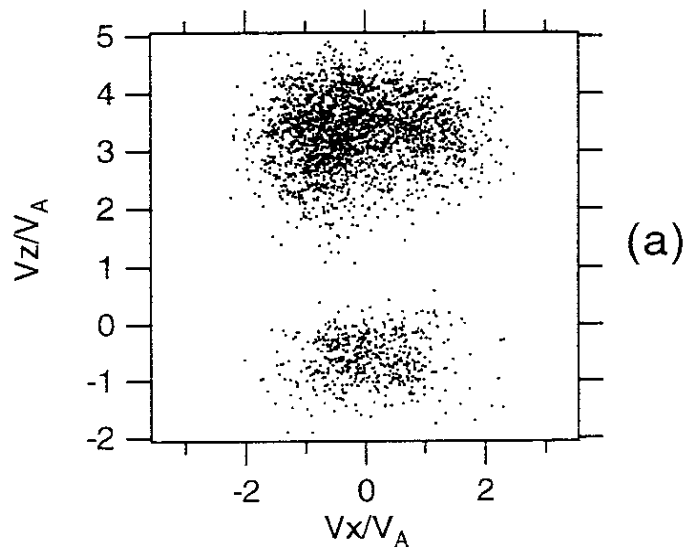
Figure 14.
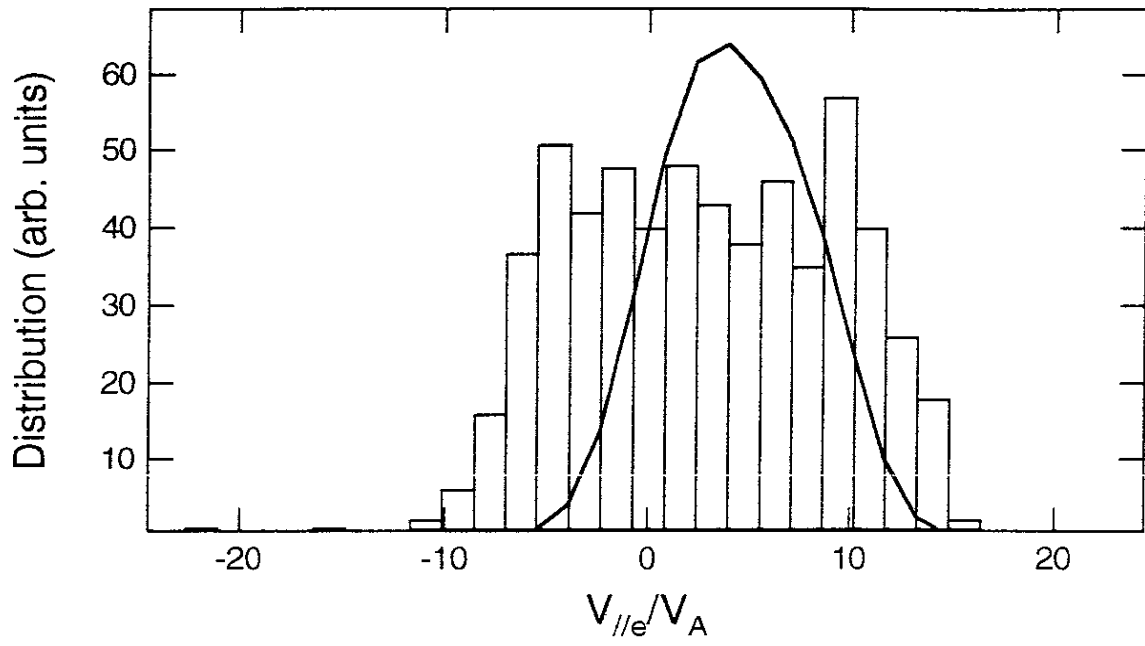
Figure 15.
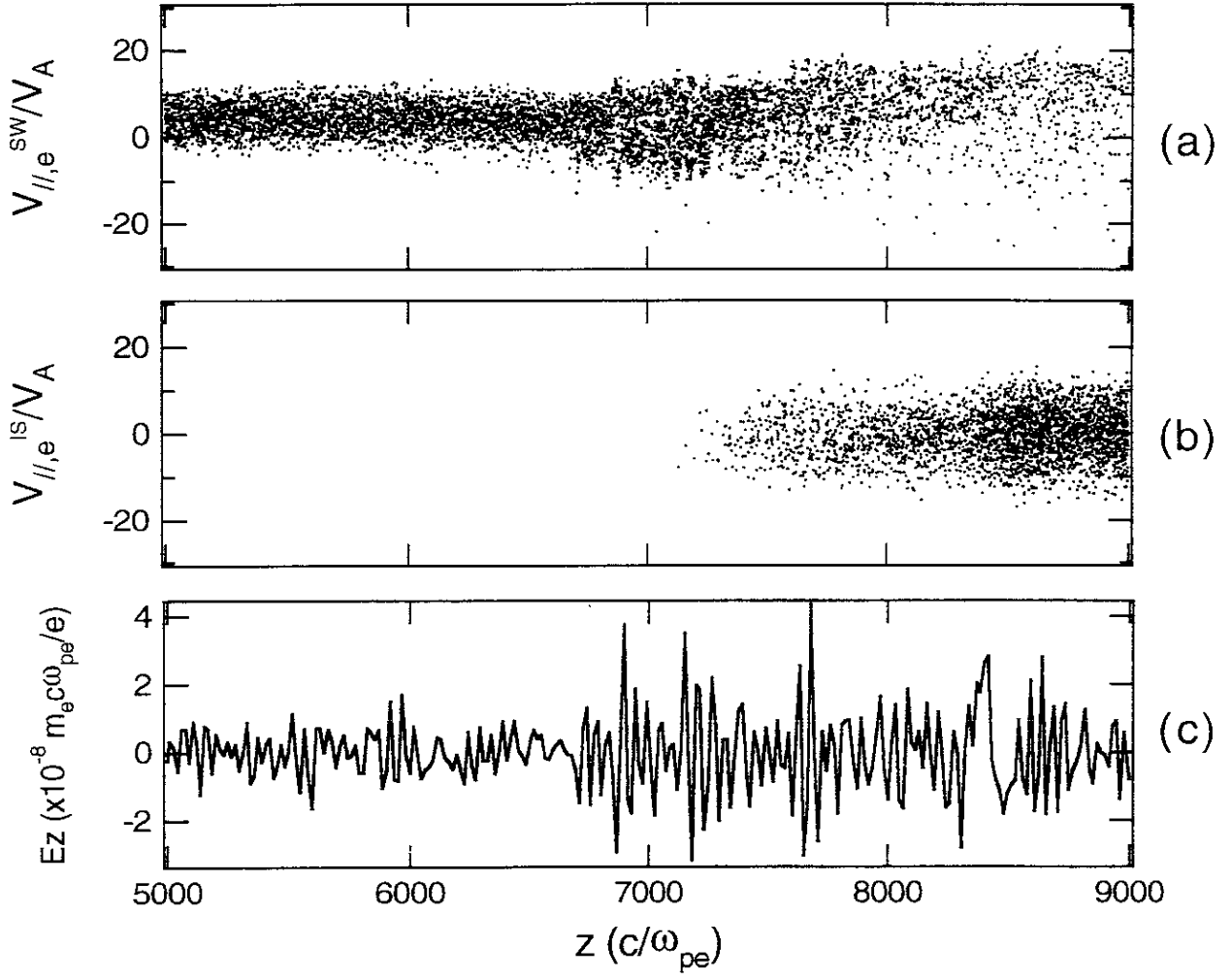
Figure 16.
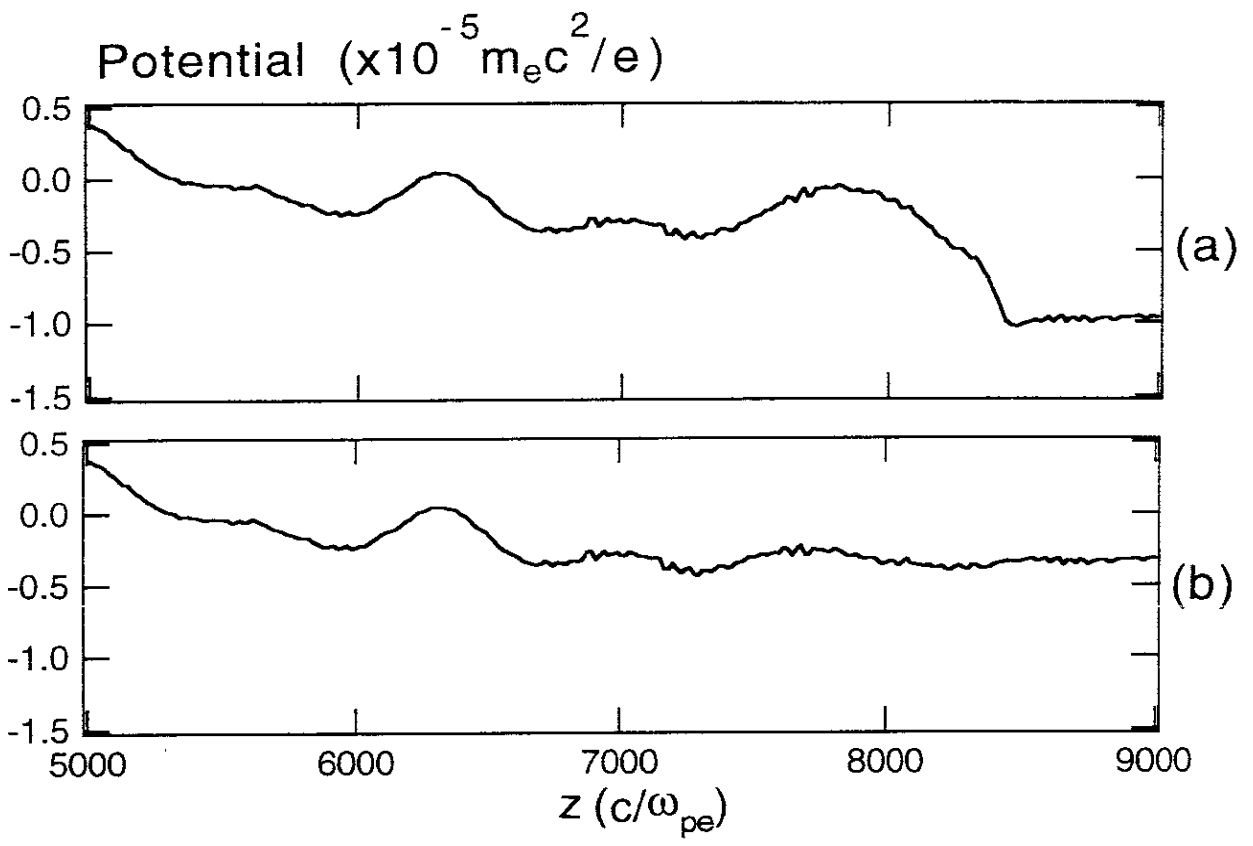
Figure 17.

Recent Issues of NIFS Series

Feb. 1995

NIFS-343   A. Ejiri, S. Sakakibara and K. Kawahata,
Signal Based Mixing Analysis for the Magnetohydrodynamic Mode Reconstruction from Homodyne Microwave Reflectometry; Mar.. 1995

NIFS-344   B.B.Kadomtsev, K. Itoh, S.-I. Itoh
Fast Change in Core Transport after L-H Transition; Mar. 1995

NIFS-345   W.X. Wang, M. Okamoto, N. Nakajima and S. Murakami,
An Accurate Nonlinear Monte Carlo Collision Operator; Mar. 1995

NIFS-346   S. Sasaki, S. Takamura, S. Masuzaki, S. Watanabe, T. Kato, K. Kadota,
Helium I Line Intensity Ratios in a Plasma for the Diagnostics of Fusion Edge Plasmas; Mar. 1995

NIFS-347   M. Osakabe,
Measurement of Neutron Energy on D-T Fusion Plasma Experiments;
Apr. 1995

NIFS-348   M. Sita Janaki, M.R. Gupta and Brahmananda Dasgupta,
Adiabatic Electron Acceleration in a Cnoidal Wave; Apr. 1995

NIFS-349   J. Xu, K. Ida and J. Fujita,
A Note for Pitch Angle Measurement of Magnetic Field in a Toroidal Plasma Using Motional Stark Effect; Apr. 1995

NIFS-350   J. Uramoto,
Characteristics for Metal Plate Penetration of a Low Energy Negative Muonlike or Pionlike Particle Beam: Apr. 1995

NIFS-351   J. Uramoto,
An Estimation of Life Time for A Low Energy Negative Pionlike Particle Beam: Apr. 1995

NIFS-352   A. Taniike,
Energy Loss Mechanism of a Gold Ion Beam on a Tandem Acceleration System: May 1995

NIFS-353   A. Nishizawa, Y. Hamada, Y. Kawasumi and H. Iguchi,
Increase of Lifetime of Thallium Zeolite Ion Source for Single-Ended Accelerator: May 1995

NIFS-354   S. Murakami, N. Nakajima, S. Okamura and M. Okamoto,
Orbital Aspects of Reachable β Value in NBI Heated Heliotron/Torsatrons; May 1995

NIFS-355   H. Sugama and W. Horton,
Neoclassical and Anomalous Transport in Axisymmetric Toroidal Plasmas

with Electrostatic Turbulence; May 1995

NIFS-356   N. Ohyabu
A New Boundary Control Scheme for Simultaneous Achievement of H-mode and Radiative Cooling (SHC Boundary); May 1995

NIFS-357   Y. Hamada, K.N. Sato, H. Sakakita, A. Nishizawa, Y. Kawasumi, R. Liang, K. Kawahata, A. Ejiri, K. Toi, K. Narihara, K. Sato, T. Seki, H. Iguchi, A. Fujisawa, K. Adachi, S. Hidekuma, S. Hirokura, K. Ida, M. Kojima, J. Koong, R. Kumazawa, H. Kuramoto, T. Minami,. M. Sasao, T. Tsuzuki, J.Xu, I. Yamada, and T. Watari,
Large Potential Change Induced by Pellet Injection in JIPP T-IIU Tokamak Plasmas; May 1995

NIFS-358   M. Ida and T. Yabe,
Implicit CIP (Cubic-Interpolated Propagation) Method in One Dimension; May 1995

NIFS-359   A. Kageyama, T. Sato and The Complexity Simulation Group,
Computer Has Solved A Historical Puzzle: Generation of Earth's Dipole Field; June 1995

NIFS-360   K. Itoh, S.-I. Itoh, M. Yagi and A. Fukuyama,
Dynamic Structure in Self-Sustained Turbulence; June 1995

NIFS-361   K. Kamada, H. Kinoshita and H. Takahashi,
Anomalous Heat Evolution of Deuteron Implanted Al on Electron Bombardment; June 1995

NIFS-362   V.D. Pustovitov,
Suppression of Pfirsch-schlüter Current by Vertical Magnetic Field in Stellarators; June 1995

NIFS-363   A. Ida, H. Sanuki and J. Todoroki
An Extended K-dV Equation for Nonlinear Magnetosonic Wave in a Multi-Ion Plasma; June 1995

NIFS-364   H. Sugama and W. Horton
Entropy Production and Onsager Symmetry in Neoclassical Transport Processes of Toroidal Plasmas; July 1995

NIFS-365   K. Itoh, S.-I. Itoh, A. Fukuyama and M. Yagi,
On the Minimum Circulating Power of Steady State Tokamaks; July 1995

NIFS-366   K. Itoh and Sanae-I. Itoh,
The Role of Electric Field in Confinement; July 1995

NIFS-367   F. Xiao and T. Yabe,

A Rational Function Based Scheme for Solving Advection Equation, July 1995

NIFS-368   Y. Takeiri, O. Kaneko, Y. Oka, K. Tsumori, E. Asano, R. Akiyama, T. Kawamoto and T. Kuroda, *Multi-Beamlet Focusing of Intense Negative Ion Beams by Aperture Displacement Technique;* Aug. 1995

NIFS-369   A. Ando, Y. Takeiri, O. Kaneko, Y. Oka, K. Tsumori, E. Asano, T. Kawamoto, R. Akiyama and T. Kuroda, *Experiments of an Intense H- Ion Beam Acceleration;* Aug. 1995

NIFS-370   M. Sasao, A. Taniike, I. Nomura, M. Wada, H. Yamaoka and M. Sato, *Development of Diagnostic Beams for Alpha Particle Measurement on ITER;* Aug. 1995

NIFS-371   S. Yamaguchi, J. Yamamoto and O. Motojima; *A New Cable -in conduit Conductor Magnet with Insulated Strands;* Sep. 1995

NIFS-372   H. Miura, *Enstrophy Generation in a Shock-Dominated Turbulence;* Sep. 1995

NIFS-373   M. Natsir, A. Sagara, K. Tsuzuki, B. Tsuchiya, Y. Hasegawa, O. Motojima, *Control of Discharge Conditions to Reduce Hydrogen Content in Low Z Films Produced with DC Glow;* Sep. 1995

NIFS-374   K. Tsuzuki, M. Natsir, N. Inoue, A. Sagara, N. Noda, O. Motojima, T. Mochizuki, I. Fujita, T. Hino and T. Yamashina, *Behavior of Hydrogen Atoms in Boron Films during H_2 and He Glow Discharge and Thermal Desorption;* Sep. 1995

NIFS-375   U. Stroth, M. Murakami, R.A. Dory, H. Yamada, S. Okamura, F. Sano and T. Obiki, *Energy Confinement Scaling from the International Stellarator Database;* Sep. 1995

NIFS-376   S. Bazdenkov, T. Sato, K. Watanabe and The Complexity Simulation Group, *Multi-Scale Semi-Ideal Magnetohydrodynamics of a Tokamak Plasma;* Sep. 1995

NIFS-377   J. Uramoto, *Extraction of Negative Pionlike Particles from a H2 or D2 Gas Discharge Plasma in Magnetic Field;* Sep. 1995

NIFS-378   K. Akaishi, *Theoretical Consideration for the Outgassing Characteristics of an Unbaked Vacuum System;* Oct. 1995